N 64 10357

Direct Measurements of Helium and Hydrogen Ion Concentration and Total Ion Density to an Altitude of 940 Kilometers

H. A. TAYLOR, JR., L. H. BRACE, H. C. BRINTON, AND C. R. SMITH

NASA, *Goddard Space Flight Center, Greenbelt, Maryland*

Abstract. A Bennett-type ion mass spectrometer and a cylindrical electrostatic probe were carried to 940 km above Wallops Island, Virginia, at midday in October 1961. The raw data from each unit (ion currents versus altitude) are presented and are interpreted in terms of helium, hydrogen, oxygen, and total ion concentration. The He⁺ and H⁺ concentrations derived from the ion mass spectrometer experiment were found to rise steeply above 350 km, He⁺ reaching a maximum value of 7×10^3/cc at 575 km and H⁺ increasing monotonically with altitude, ultimately reaching about 1.5×10^3/cc near apogee. These data are used with the O⁺ concentrations derived from the electrostatic probe data to calculate the atmospheric temperature, the mean ion mass, and the total ion concentration as functions of altitude. The temperature of the upper F region was found to be $1235° \pm 40°$K. The mean ion mass decreased from 16 AMU at 400 km to 12 AMU at apogee where it was decreasing rapidly. The measured ion distributions and those predicted by the theories of hydrostatic diffusion and ion-atom interchange are compared.

Introduction. At 1740 GMT (1240 local time) on October 10, 1961, an Argo-D4 rocket (NASA 8.23) was launched eastward into the ionosphere above Wallops Island, Virginia, carrying a Bennett-type ion mass spectrometer and a cylindrical electrostatic probe to an altitude of 940 km and a range of 1200 km. The mass range of the spectrometer had been selected to permit optimum resolution of both hydrogen and helium ions which had been postulated for the upper F region by *Nicolet* [1961] and have since been inferred from rocket and satellite measurements [*Hanson,* 1962; *Bourdeau et al.,* 1962]. The successful operation of the spectrometer permitted the first high resolution direct measurements of the H⁺ and He⁺ concentrations in the exosphere. The electrostatic probe was included in the payload to permit a measurement of the total ion density and the electron temperature.

The equipment was placed aboard the vehicle as shown in Figure 1, the ion spectrometer looking forward during rocket ascent and the cylindrical probe protruding from the side of the payload. In flight, the rocket spun at a rate of 1 rps about its longitudinal axis with a precession cone half-angle less than 1°. The spin axis, essentially in the plane of the trajectory, made an angle of 15° with the vertical. During the flight approximately 600 spectrums and 5000 probe volt-ampere characteristics were recorded.

In addition to the spectrometer and probe, an optical aspect sensor was included in the payload to permit determination of sensor orientation; this information aided in the conversion of spectrometer currents to ambient ion concentrations. Ionosonde measurements were recorded at Wallops Island throughout the flight to provide electron density data up to the F_2 maximum.

The ion spectrometer. The Bennett radio-frequency spectrometer was similar in design to that flown at Wallops Island by *Taylor and Brinton* [1961]. However, the mass range and sensitivity were modified to permit unambiguous detection of ions in the mass range of 1–5 AMU. The theory of operation of the spectrometer together with some of the technical details of this experiment has been presented previously [*Taylor et al.,* 1962]. Although the theory is not elaborated upon here, it is important to consider several basic parameters of the measurement and their influence on the interpretation of the data.

The basic relationship between resonant mass, tube geometry, and potentials applied to the spectrometer grids is given by the equation

$$M = 0.266(|V_A| + |V_B|)/S^2 F^2 \quad (1)$$

where M is the resonant mass, V_A is the instan-

taneous value of the negative sawtooth accelerating potential, V_B is a positive bias potential, S is the spacing between grids in the RF analyzer stages, and F is the frequency of the RF potential applied to the analyzer sections. For this flight a three-stage, 5–3 cycle tube was used, with $V_B = 20$ volts dc, $S = 0.75$ cm, $F = 5$ Mc/s, and $V_A = 0$ to -270 volts dc. This provided a mass range of approximately 1 to 5 AMU with a resolution of 0.5 AMU. This spectrum was analyzed at the sweep rate of V_A, which was 1 cps.

An important parameter not contained in (1) is the stopping potential V_S, which regulates the number of ions reaching the collector. In this process V_S controls the efficiency of the spectrometer and also determines the ratio of fundamental to harmonic ion content. The effectiveness of V_S is dependent on the energy gained by ions in traversing the spectrometer and is thus also dependent on energy that ambient ions may gain owing to the effects of external potentials and vehicle velocity.

To insure adequate efficiency and sensitivity to harmonic ions, the V_S level was stepped automatically through an appropriate range of voltage. The harmonic ions detected were analyzed by a technique similar to that developed by *Johnson* [1958] to confirm the identification of
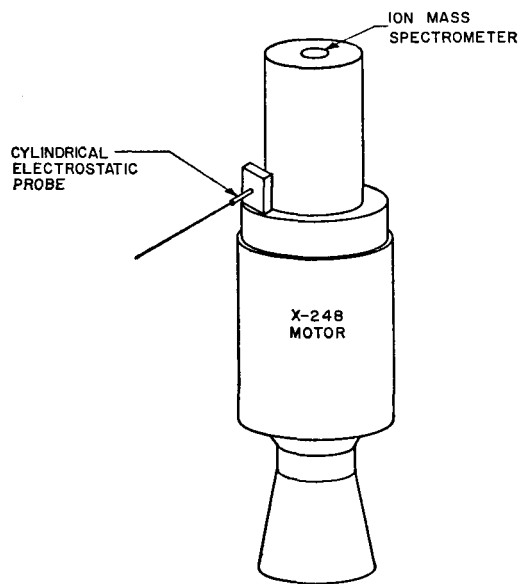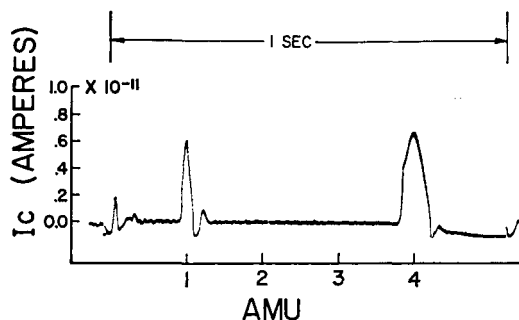

ION SPECTRUM– NASA 8.23

Fig. 2. A sample positive ion spectrum recorded near apogee on NASA 8.23.

the fundamental ions as 1 AMU and 4 AMU. Although there was some evidence in the data of an apparent lowering of the effective value of V_S that has not as yet been accounted for in terms of measured experimental parameters, the relationships between fundamental and harmonic ions observed in the flight data agree favorably with both theoretical predictions and laboratory calibrations.

A photograph of a segment of the flight data, recorded near apogee, is shown in Figure 2. Only two fundamental ion current peaks, H^+ and He^+, were observed during the flight. The raw ion currents I_c measured at the collector of the spectrometer during ascent are plotted in Figure 3. As is indicated by the error bars, the spread, or deviation, in the raw current data points is slight, as might be expected because of the high degree of aspect stability experienced during flight.

Ion currents collected during descent when the spectrometer was exposed to the the wake of the payload are not presented. Although certain parts of the descent data compare favorably with the ascent data, the difficulties inherent in the interpretation of the wake effect preclude the inclusion of the descent data.

Conversion of ion currents to densities requires the determination of over-all experimental sensitivity, which is a function of vehicle potential and velocity, plasma sheath configuration adjacent to the orifice, spectrometer efficiency, and amplifier sensitivity. Both the limiting amplifier sensitivity and spectrometer efficiency were measured directly in the laboratory. These measured values, together with the best estimates of the other effects, have been

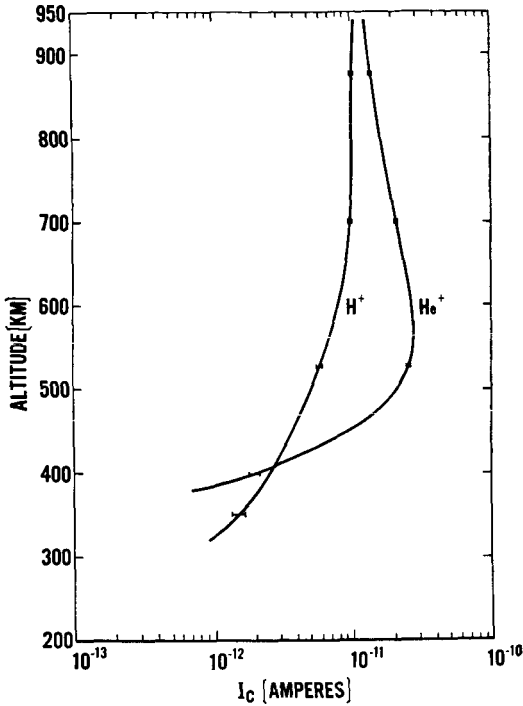Fig. 1. Locations of equipment on NASA 8.23.

Fig. 3. Helium and hydrogen ion currents detected by the ion mass spectrometer.

combined to determine a maximum sensitivity of approximately 10 ions/cc. The relationships of those parameters which were not subject to direct measurement, together with the resulting technique for determination of ion density, are discussed in detail in appendix 1.

It is interesting to consider what observations can be made from the H^+ and He^+ current distribution curves if a simplified conversion to ion density is performed. The part of the trajectory where the perturbing influences of velocity and plasma sheath are most easily interpreted is at peak altitude. At that point the densities attributed to H^+ and He^+ are estimated to be 1.4×10^3 ions/cc and 3.2×10^3 ions/cc, respectively. Figure 4 is a plot of ascent density distributions obtained from the current distributions as discussed in appendix 1. Although the current curves are now plotted as densities, the distributions remain identical to the current profiles of Figure 3, since no modifying functions have been applied to the original curves.

As is discussed in appendix 1, it is believed that the most accurate conversion of collector current I_c to the number densities $n(H^+)$ and

$n(He^+)$ may ultimately require a simultaneous solution of the effects of velocity, sheath, and effective orifice area, which, to date, have yielded only to separate analyses. Although it is recognized that these unsolved relationships may modify the shape of the derived composition, it is believed that the attracting field of the orifice grid was the predominating influence, and that the measured current distributions closely represent the ambient ion distributions. With these qualifications then, the H^+ and He^+ concentration profiles will be compared in later sections with the density data obtained by the electrostatic probe.

The electrostatic probe. The cylindrical probe used in this flight was nearly identical to one described by *Spencer et al.* [1962] which was carried as a secondary experiment on two flights of a series of ejected instrument packages launched into the F region. Figure 5 shows a block diagram of the measurement system employed. The metallic payload mounting and instrument housings acted collectively as a plasma reference electrode from which a sawtooth voltage was applied to both the guard and collector
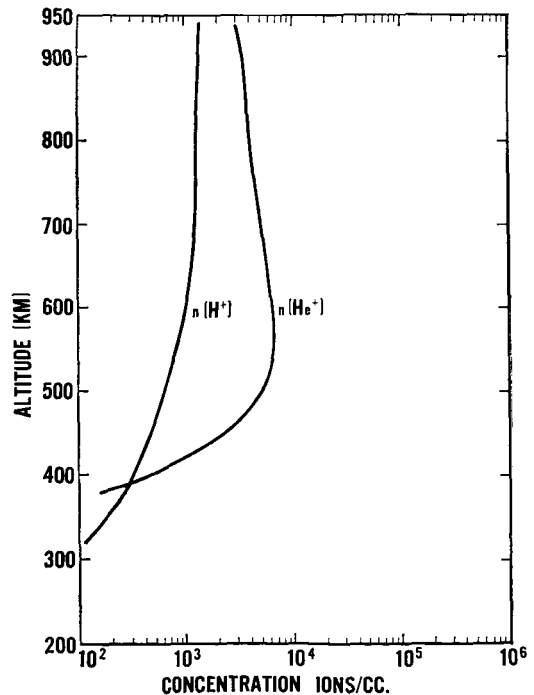

Fig. 4. Helium and hydrogen ion concentration profiles derived from the ion mass spectrometer currents shown in Figure 3.
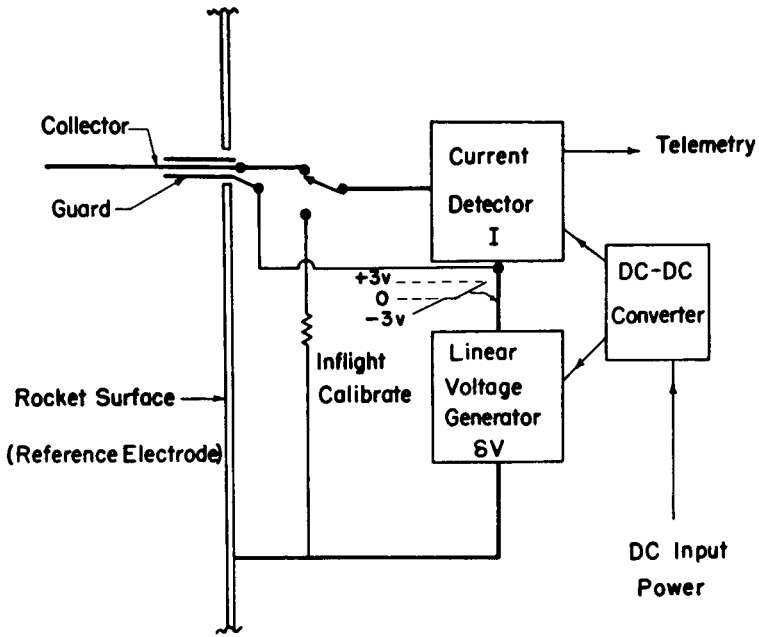
Fig. 5. Block diagram of the electrostatic probe.

elements of the probe sensor. Figure 6 is a photograph of a one-second section of telemetry record showing a series of volt-ampere characteristics recorded at 510 km during ascent. In the central part of the photograph, the ionosphere measurements are interrupted by a brief period of inflight current-calibration during which the probe was electrically disconnected and a known resistance substituted into the measurement circuit. The resulting current wave form was used to calibrate the current channel. Diode limiting at the output of the detector

was used to prevent negative currents from driving the telemetry out of band. At the left and right of the calibration wave forms, the positive parts of a series of cylinder current characteristics are displayed. These represent the net current ($I_{net} = I_p + I_e$, the sum of the ion and electron currents) that was collected as the applied voltage was swept through the range of +2 volts to −3 volts, pausing briefly at zero volts for purposes of reference. As is shown in the calibration, the sensitivity of this particular channel was selected to resolve only net positive
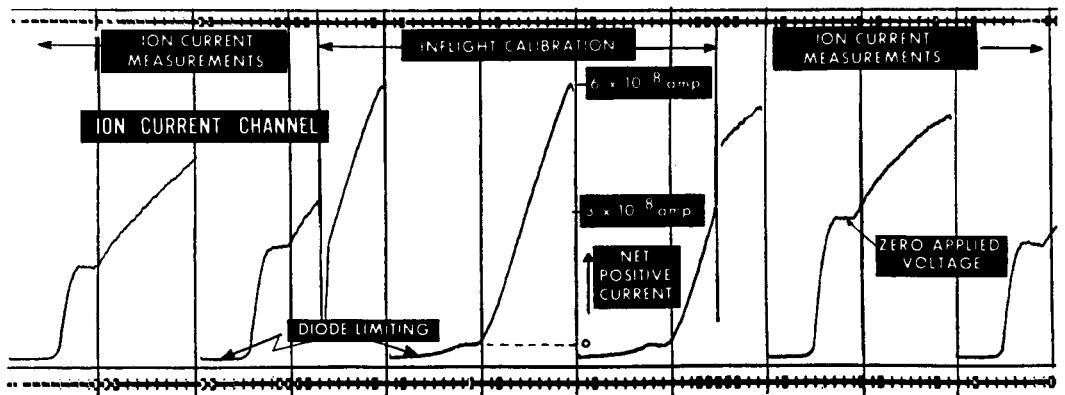

Fig. 6. Photograph of a segment of telemetry record showing electrostatic probe ion currents measured at 510 km, and an inflight current calibration.

currents. Note that at zero applied voltage a net positive current flows to the probe (indicating that the collector was being held more negative than its equilibrium potential). As the applied voltage was swept negative, the ambient electrons were entirely rejected and the probe current was due to positive ions alone. Conversely, for positive applied voltages the electron current quickly exceeded the ion current, thus driving the net current negative and out of the range of this detector. A second detector, having the correct sensitivity to resolve the much larger electron currents, was to be used periodically, but a programmer failure prevented its use and permitted the ion current detector to operate full time. This improved the resolution of the ion current data but hampered the analysis of the current characteristics for electron temperature.

Figure 7 shows a running mean of the maximum ion currents (measured at maximum negative voltage) recorded throughout the flight. The times of F_2 passage are evident in the current maximums at 1743 and 1757 GMT on ascent and descent, respectively. It should be noted that these positive currents result not only from the collection of positive ions but include a small component due to photoemission, i.e. ejection of electrons from the collecting surface as the result of solar extreme ultraviolet radiation and X-ray impingement. The photocurrent has been evaluated by means of the small jump-

discontinuity it produces in the current as the rocket spin carries the probe through the shadow of the payload structure. At apogee, where the total positive current had fallen to 8×10^{-9} ampere, the photocurrent was found to be 2×10^{-9} ampere. This value is in acceptable agreement with rocket measurements of *Hinteregger et al.* [1959] of photoemission which, when translated to the geometry and area of the cylindrical collector, correspond to a value of about 3.5×10^{-9} ampere. The decrease in solar activity since the time of Hinteregger's measurements accounts for the lower value of photocurrent observed on this flight. This photocurrent was a constant but negligible factor over much of the altitude range covered (less than 1 per cent of the net positive current at the F_2 maximum) but became significant near apogee where it amounted to as much as 25 per cent of the measured positive current. The current data presented in Figure 7 have not been corrected for photocurrent; however, this correction was made before conversion to ion concentration.

Conversion of the currents shown in Figure 7 to the related total ion concentration, as discussed in appendix 2, requires an assumption about the ion species present or an independent determination of it. Below 450 km O^+ is the dominant F-region ion [*Taylor and Brinton,* 1961]. Above 450 km, however, the ion mass spectrometer data show that He^+ and H^+ become important constituents. The higher mean veloci-
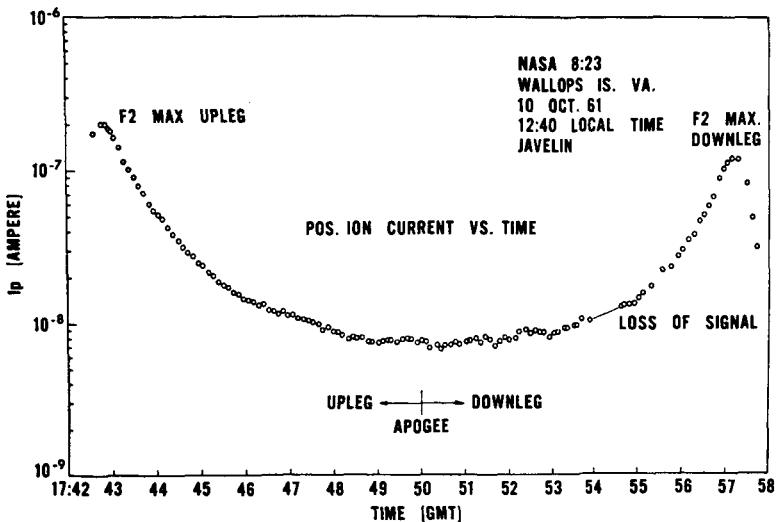

Fig. 7. Positive ion current to the electrostatic probe throughout the flight.
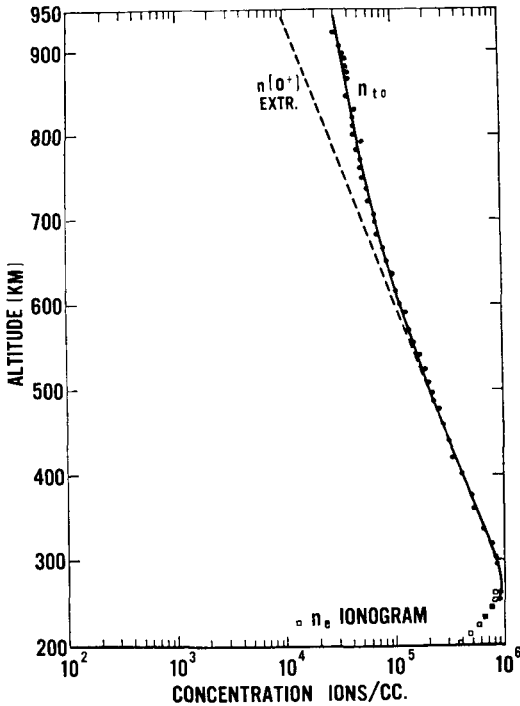
Fig. 8. Total ion concentration, n_{to}, derived from the electrostatic probe currents by assuming oxygen ions only, and the oxygen ion concentration, $n(O^+)$, derived by extrapolating the n_{to} measured between 350 and 500 kilometers.

ties of these light ions produce a greater positive current to the probe than a like number of oxygen ions and, if not considered, will lead to a total ion concentration that is too high. As a first approximation, however, it is instructive to assume that only O^+ is present and to generate an 'upper limit' total concentration, n_{to}, from the ion current data. The resulting ion concentration profile is shown in Figure 8. The ionosonde values of n_e, which are believed most accurate, are shown for comparison. The agreement between n_e and n_{to} near the F_2 maximum tends to demonstrate the accuracy of equation 12 in appendix 2.

It is presumed that the part of the profile below 450 km represents a hydrostatic distribution of O^+, the only ion present in significant numbers. Thus, if thermal equilibrium is assumed, the observed scale height of 147 ± 5 km leads to a temperature of 1235° ± 40°K. An extension of the O^+ distribution to higher altitudes can be carried out rigorously by means

of the method outlined by *Bauer* [1962] and *Hanson* [1962]. For the values of $n(H^+)$ and $n(He^+)$ observed by the spectrometer, however, $n(O^+)$ is sufficiently predominant that a linear extrapolation with geometric altitude approximates the hydrostatic distribution. This linear extrapolation of $n(O^+)$ is shown as the dashed line in Figure 8. When we compare $n(O^+)$ and n_{to}, the effect of the helium and hydrogen ions upon the probe current becomes evident just above 500 km and is seen to increase with altitude.

Interpretation of the combined results. The helium and hydrogen ion concentrations can be combined with the oxygen ion concentration values to permit a check upon the consistency of the two sets of experimental data shown in Figures 4 and 8. If we assume that no other ions are present, simple addition of the individual ion concentrations, $n(H^+)$, $n(He^+)$, and $n(O^+)$, provides the total ion concentration n_{t1} shown in Figure 9. The same values can be used in equation 12 to adjust the upper limit total con-
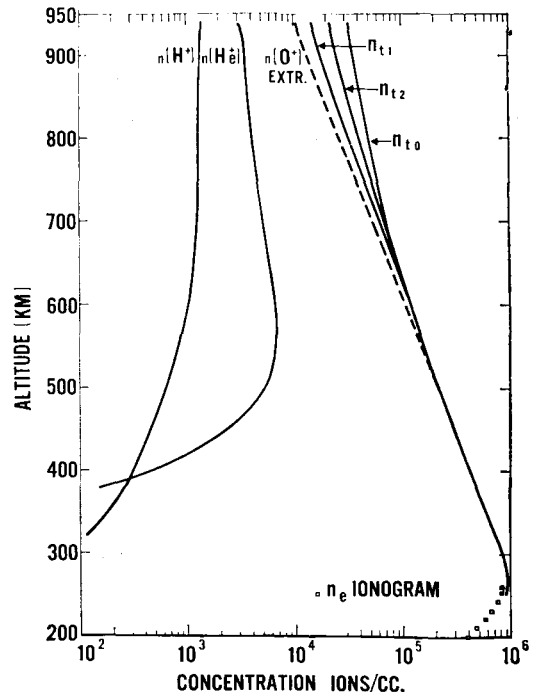

Fig. 9. Composite ion concentration profiles including total ion density, n_{t1}, obtained by adding $n(H^+)$, $n(He^+)$, and $n(O^+)$; and n_{t2} derived by correction of n_{to} for the presence of the lighter ions.

centration, n_{to}, for the presence of helium and hydrogen ions. The resulting values of total concentration are labeled n_{t2} in Figure 9. Although n_{t1} and n_{t2} are not arrived at entirely independently, the agreement between them demonstrates a satisfying degree of consistency in the flight data from the two experiments. From the electrostatic probe data alone, we would postulate slightly greater concentrations of the light ions than is indicated by $n(H^+)$ + $n(He^+)$; however, the agreement between n_{t1} and n_{t2} is within the combined probable errors of the measurements and the extrapolation method employed in obtaining $n(O^+)$.

The same parameters can be used with (2) to obtain a profile of the mean ion mass m_i that existed in the ionosphere during this flight as shown in Figure 10.

$$m_i = (1/n_t) \sum_k n_i m_i \qquad (2)$$

Note that the mean ion mass had decreased from 16 AMU below 400 km to 12 AMU at apogee and was decreasing rapidly there.

Discussion and conclusions. Probably the most significant result of these measurements is the detection of helium and hydrogen ions in the upper F region in substantially the amounts predicted [*Nicolet,* 1961; *Hanson,* 1962; *Bates and Patterson,* 1962]. However, the occurrence of a helium ion maximum at 575 km is not in accord with ion diffusion theory [*Mange,* 1960; *Bauer,* 1962] which predicts that the helium maximum should occur somewhat above the transition level where it becomes the dominant ion. Both the theory and this experiment indi-

cate that the transition level occurs above 1000 km for an ionosphere temperature of 1235°K. We do not interpret the difference between the experimental and theoretical helium distributions as indicating an inadequacy in the diffusion theory, but regard this as evidence of additional geophysical effects that influenced the vertical distribution of ions at the time of this flight. For example, the geomagnetic field and field-aligned irregularities, when present, modify the charged particle profiles to various degrees, depending on the latitude and local ionospheric conditions.

The temperature derived from the electrostatic probe data is in agreement with the *Harris and Priester* [1962] model of gas temperature derived for similar local times and levels of solar activity.

The altitude at which He^+ was first detected, and the steep gradient immediately above, are in agreement with *Hanson's* [1962] predictions based on an ion-atom interchange process between He^+ and N_2. Bates and Patterson have since shown that this process is more likely to involve O_2 than N_2. The comparison of $n(He^+)$ obtained from this flight with the distributions predicted by Bates and Patterson permits us to infer that the rate coefficient for the ion-atom interchange process lies between 3.7×10^{-11} and 2.0×10^{-10} cm³/sec.

Appendix 1

Conversion of Spectrometer Collector Current to Ion Density

The conversion of the spectrometer collector current to positive ion density involves parameters that are effective inside the sensor as well as those that control the effective collection area associated with the sensor orifice.

A laboratory calibration of the internal sensor parameters is performed to determine the relationship

$$I_e = kI_o \qquad (3)$$

where the spectrometer efficiency $k = \alpha\phi$; α is the combined electrical transparency of the grids determined by measuring the attenuation of an ion beam in passing through a grid system; ϕ is the current efficiency of the analyzer system obtained analytically, and I_o is the known ion input current measured at the spectrometer
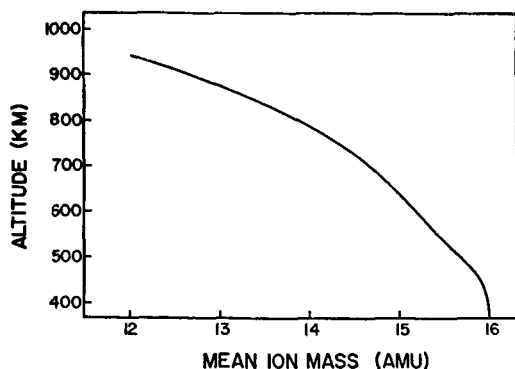

Fig. 10. Mean ion mass derived from $n(H^+)$, $n(He^+)$, and $n(O^+)$ values given in Figure 9.

orifice. Values of k determined from direct laboratory measurements of I_o and I_o are in agreement with theoretical predictions of over-all efficiency. This calibration, performed with a controlled beam of positive ions directed along the spectrometer axis, did not include the simulation of effects external to the orifice.

The external effects influencing the collected currents were not subject to direct measurement. To a first-order approximation, the current to the orifice grid can be determined from the expression for a planar probe [*Mott-Smith and Langmuir*, 1926]:

$$I_o = n_i e a A / 2 \sqrt{\pi} \qquad (4)$$

where n_i is the ion density in ions per cubic centimeter, a is the most probable ion velocity, and A is the area of the orifice grid. In flight, however, the quantity I_o was influenced by two perturbing factors; first, the negative drawing-in potential E_o applied to the orifice grid to increase the over-all ion sensitivity; and second, the rocket velocity V_r and angle of attack. These factors combined to modify the input current flow, resulting in the relationship

$$I_o = (n_i e a A / 2 \sqrt{\pi}) f(E_o, V_r) \qquad (5)$$

Because of the orifice geometry and the resulting fringing field surrounding the orifice grid, we must consider the factors A and $f(E_o, V_r)$ in (5) together to evaluate the resultant effective collection area A_{eff}.

Since the function $f(E_o, V_r)$ was not subject to direct measurement, the value of A_{eff} has been approximated at peak altitude, where the correction for velocity, aspect, and composition is believed to be most reliable. Because of the strong drawing-in field of the first grid (-10 volts) and the relatively low velocity at peak altitude, the term $f(V_r)$ is dropped. An approximation of $f(E_o)$ based on a consideration of the orifice geometry and fringing field results in $A_{eff} = 3A$.

The resulting expression for ion density at peak is

$$n_i = 2 \sqrt{\pi} I_c / k e a A_{eff} \qquad (6)$$

and by substituting $k = 1.5$ per cent, $A_{eff} = 25.6$ square centimeters, together with appropriate values of I_o and a, we determined the quantities for $n(\text{H}^+)$ and $n(\text{He}^+)$ at peak.

The energy gained by ambient hydrogen and helium ions because of the relative velocity of the vehicle is of the order of their thermal energies, whereas the energy imparted to the ions by the drawing-in potential is approximately a factor of 100 times the thermal energy. It is assumed, therefore, that effects of vehicle velocity on the collection of light ions, although not constant with altitude, are very small compared to the presumably constant effect of the drawing-in potential. On the basis of these assumptions, then, the ion density distributions of Figure 4 have been obtained by applying (6) to the measured ion current distributions of Figure 3.

APPENDIX 2

ELECTROSTATIC PROBE THEORY

If the cylindrical collector were stationary at each point of measurement in the ionosphere, the ion currents recorded throughout the flight would be related in a well-known way to the ion number n_p, mass m_p, charge e, and temperature T_p, as well as the area A and voltage V of the collector. This relationship is expressed for a given ion species by Langmuir's equation for stationary cylindrical probes [*Mott-Smith and Langmuir*, 1926].

$$i_{ps} = A n_p e (k T_p / 2 \pi m_p)^{1/2}$$
$$\cdot (2 / \sqrt{\pi})(1 + e V / k T_p)^{1/2} \qquad (7)$$

Since the term $e V / k T_p$ is normally much greater than 1, equation 7 can be written

$$i_{ps} = A n_p e (2 e V / \pi^2 m_p)^{1/2} \qquad (8)$$

If more than one ion species is present, the current due to each may be considered separately so that the total current is

$$i_{ps} = A e (2 e V / \pi^2)^{1/2} \sum_i n_i / \sqrt{m_i} \qquad (9)$$

For a ternary mixture of hydrogen, helium, and oxygen ions such as that observed on this flight, (9) becomes

$$i_{ps} = A e \left(\frac{2 e V}{\pi^2 m_{\text{H}^+}} \right)^{1/2}$$
$$\cdot \left[n(\text{H}^+) + \frac{n(\text{He}^+)}{2} + \frac{n(\text{O}^+)}{4} \right] \qquad (10)$$

In rocket application, however, the probe moves through the plasma at velocities comparable to the mean ion velocities; therefore an additional flux of ions is intercepted or swept out by the collector. In the limit of high velocity, the collector sweeps out ion current proportional to the total number of ions present n_t, their charge e, the translational velocity of the probe W, and the area of the collector projected in the direction of motion $A \sin \theta$. Thus the ion current swept out is given by the equation

$$i_{pw} = n_t e W A \sin \theta \qquad (11)$$

where θ is the angle between the probe axis and the velocity vector.

The total ion current to the collector can be viewed as the sum of the random current and the current that is swept out, as given by (12).

$$i_p = i_{ps} + i_{pw}$$
$$= Ae[(2e\,V/\pi^2)^{1/2} \sum_i n_i / \sqrt{m_i} + n_t\,W \sin \theta] \qquad (12)$$

This is an oversimplified description of the current collection process, since it assumes that the stationary current (equation 10) and the high-velocity expression (equation 11) apply independently and therefore can be added. Furthermore, the degree of inaccuracy resulting from this assumption is variable, since it depends on both the vehicle velocity and the particular ion species present. For example, the rocket velocity in this flight was always less than the most probable hydrogen ion velocity but exceeded that of the oxygen ions through much of the altitude range. In spite of this, considerable justification for its use, particularly at higher velocities, derives from the agreement evident between the resulting F_2-region ion concentrations and the corresponding electron concentrations derived from the ionosonde records. In this region, i_{ps} and i_{pw} are comparable in magnitude. At higher altitudes, the velocity is less and (12) reduces to (10).

The spinning motion of the rocket permits a simplification of the data analysis. Twice during each rotation, the rocket spin brings the collector perpendicular to the velocity vector W. At these orientations $A \sin \theta$ reduces in effect to A, and the full ion sweeping effect generates maximums in the successive ion current characteristics that in turn permit this orientation to be easily recognized. The values of ion current measured each time the collector assumed this orientation are shown in Figure 7. After correcting for photoemission, we used these currents with (12) to derive the total ion concentration profile given in Figure 8.

REFERENCES

Bates, D. R., and T. N. L. Patterson, Helium ions in the upper atmosphere, *Planetary Space Sci., 9,* 599–605, 1962.

Bauer, S. J., On the structure of the topside ionosphere, *J. Atmospheric Sci., 19,* 276–278, 1962.

Bourdeau, R. E., E. C. Whipple, Jr., J. L. Donley, and S. J. Bauer, Experimental evidence for the presence of helium ions based on Explorer 8 satellite data, *J. Geophys. Res., 67,* 167–275, 1962.

Hanson, W. B., Upper atmosphere helium ions, *J. Geophys. Res., 67,* 183–188, 1962.

Harris, I., and W. Priester, Time-dependent structure of the upper atmosphere, *J. Atmospheric Sci., 19,* 286–301, 1962.

Hinteregger, H. E., K. R. Damon, and L. A. Hall, Analysis of photoelectrons from solar extreme ultraviolet, *J. Geophys. Res., 64,* 961–969, 1959.

Johnson, C. Y., Mass determination of ions detected by Bennett ion RF mass spectrometer, *J. Appl. Phys., 29,* 740–741, 1958.

Mange, P., The distribution of minor ions in electrostatic equilibrium in the high atmosphere, *J. Geophys. Res., 65,* 3833–3834, 1960.

Mott-Smith, H. M., and I. Langmuir, The theory of collectors in gaseous discharges, *Phys. Rev., 28,* 727–763, 1926.

Nicolet, M., Helium, an important constituent in the lower exosphere, *J. Geophys. Res., 66,* 2263–2264, 1961.

Spencer, N. W., L. H. Brace, and G. R. Carignan, Electron temperature evidence for nonthermal equilibrium in the ionosphere, *J. Geophys. Res., 67,* 157–175, 1962.

Taylor, H. A., Jr., and H. C. Brinton, Atmospheric ion composition measured above Wallops Island, Virginia, *J. Geophys. Res., 66,* 2587–2588, 1961.

Taylor, H. A., Jr., H. C. Brinton, and C. R. Smith, Instrumentation for atmospheric composition measurements, *Proc. 8th Ann. Aero-Space Symp.,* pp. 1–14, Instrument Society of America, Washington, 1962.